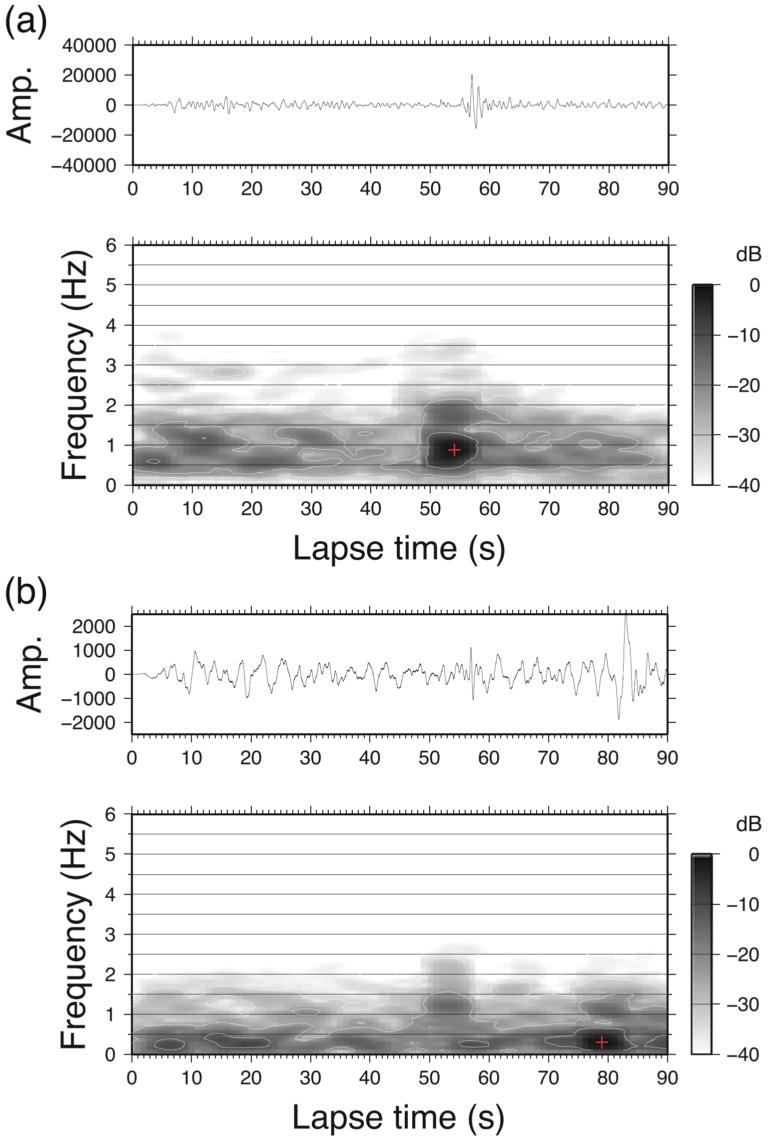

Fig. 4 Spectrograms including PcP and PKiKP. Raw seismograms and spectrograms of event 3 for **a** PcP and **b** PKiKP recorded at station IKTH. Spectrogram scaling is in decibels (dB). The predicted arrival times of PcP and PKiKP are located at a lapse time of 50 s

and PcP. On the right side, G represents the geometrical spreading factor; f_0 (=1 Hz) and f are reference and observed frequencies, respectively; T_{PK} and T_{KP} are the transmission coefficients at the CMB; and R_{PP} and R_{KK} denote reflection coefficients at the CMB and ICB, respectively. The reflection coefficient R_{KK} at the ICB is estimated from the corrected spectral ratios by considering the terms of the reflection and transmission coefficients at the CMB, the geometrical spreading factor, and anelastic parameters, which are calculated using ak135 (Kennett et al. 1995):

$$(R_{\mathrm{KK}})_{\mathrm{estimated}} = \left[\left(\frac{A_{\mathrm{PKiKP}}}{A_{\mathrm{PcP}}}\right)_{\mathrm{corrected}}\right] \Big/ \left[\frac{T_{\mathrm{PK}} T_{\mathrm{KP}}}{R_{\mathrm{PP}}} \frac{G_{\mathrm{PKiKP}}}{G_{\mathrm{PcP}}} \frac{\exp(-\pi f_0 t^*_{\mathrm{PKiKP}})}{\exp(-\pi f_0 t^*_{\mathrm{PcP}})}\right]. \tag{2}$$

We converted the spectral ratios to reflection coefficients as a function of frequency. To the first order, geometric spreading is constant with respect to frequency under a ray-theoretical assumption. The reflection and transmission coefficients were then calculated for planar boundaries. The correction of the attenuation factor using t^* gives a smooth exponential variation with frequency.

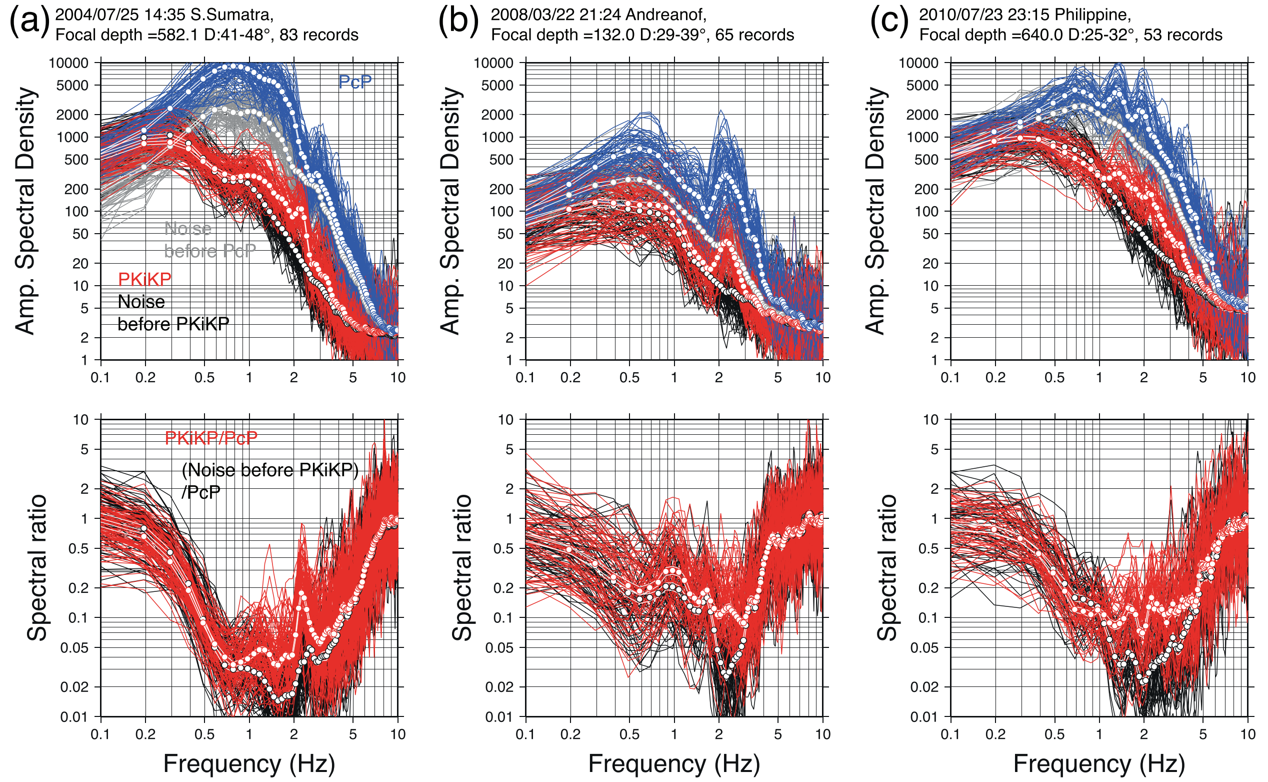

Fig. 5 Spectra of PcP and PKiKP and spectral ratios of PKiKP/PcP. Individual PKiKP, PcP, noise spectra, and PKiKP/PcP spectral ratios for **a** event 3, **b** event 6, and **c** event 11 (see Fig. 2 for the event location). (*Top row*) Spectra of PcP (*blue lines*) and PKiKP (*red lines*), noise in the 20 s window prior to PcP (*gray lines*), and noise in the 20 s window prior to PKiKP (*black lines*). *Open circles* are average spectral amplitudes for PcP, PKiKP, noise prior to PcP, and noise prior to PKiKP at each frequency. (*Bottom row*) Spectral ratios of PKiKP/PcP (*red lines*) and noise before PKiKP/PcP (*black lines*). *Open circles* are average values of spectral ratios at each frequency

Thus, these corrections will not result in any spectral holes or peaks.

To reduce the unwanted effect of the CMB on the PcP spectra, the spectral ratios of PcP/P were examined. Similar to the above procedure, we estimated the P wave reflection coefficients at the CMB as a function of frequency. The obtained reflection coefficients did not always coincide with theoretical values due to the uncertainty in focal mechanisms, large differences in P and PcP take-off angles, and other unknown causes. Thus, we corrected only the fluctuations in the reflection coefficients around the average values in the frequency range 1–3 Hz. The reflection coefficients at the ICB are multiplied by the fluctuations in reflection coefficients at the CMB, which can result in either amplifying an apparently small PKiKP/PcP due to a large peak in the PcP spectrum or reducing a large PKiKP/PcP due to a small peak in the PcP.

Results

A summary of frequency-dependent ICB P wave reflection coefficients, as derived from Eqs. (1) and (2), is shown in Fig. 6. Panels are sorted by increasing incidence angle at the ICB; we refer to each panel hereafter as result *n*, where *n* stands exclusively for panel number. Figure 7 summarizes frequency-dependent P wave reflection coefficients at the CMB derived from PcP/P spectral ratios. In Fig. 8, these are used to correct the reflection coefficients at the ICB (Fig. 6). These corrected values are used in finite difference modeling and subsequent interpretation.

The frequency characteristics of the ICB reflection coefficients are quite complex, even in a narrow effective signal band (Fig. 8). Roughly speaking, peaks in reflection coefficients appear around 2 Hz (results 8, 9, and 10) and 3 Hz (result 3), and holes are observed around 1 Hz (results 2, 3, and 4) and 3 Hz (result 10). Although the discrimination is still qualitative, we recognize four general categories of frequency-dependent characteristics: (i) a flat variation, where fluctuations in the relative strengths of peaks and holes are between half and double those of the theoretical reflection coefficients (results 1, 5, 6, 7, and 11); (ii) a distinct single hole in each reflection coefficient spectrum (results 2 and 4); (iii) a strong single peak in each spectrum (results 8 and 9);

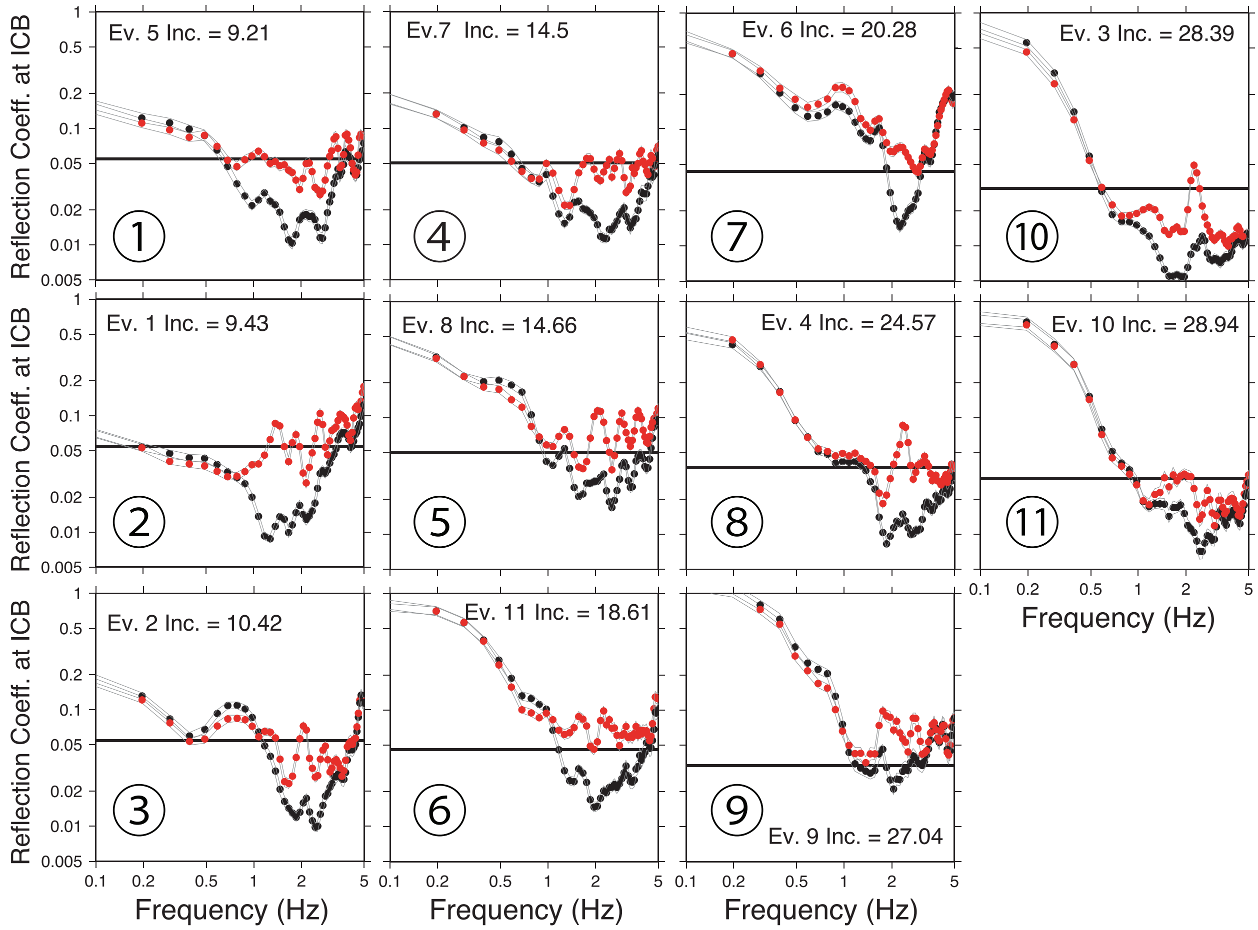

Fig. 6 P wave reflection coefficients at the ICB. P wave reflection coefficients at the ICB as a function of frequency, estimated from PKiKP/PcP spectral ratios (*red circles*) and noise/PcP (*black circles*). *Thin lines* show the upper and lower bounds of standard errors. *Thick lines* are theoretical values of reflection coefficients calculated using ak135 (Kennett et al., 1995). *Encircled numbers* are "result numbers," arranged by ascending incidence angle

and (iv) a strong peak and hole in the same spectrum (results 3 and 10).

The geographical distribution of these categories is plotted in Fig. 9. The diameters of the 1 and 2 Hz Fresnel zones for PKiKP are approximately 80 and 60 km at the ICB, respectively. This is equivalent to the area of PKiKP reflection points at the ICB that is covered by a single event and all stations that detect PKiKP. This result suggests that our averaging within each region number is meaningful, but it is not appropriate in discussing lateral variations in individual measurements within each region. Although the sampling areas are sparse, we note a tendency of frequency peaks in reflection coefficient spectra to be most observable at low latitudes (results 8, 9, and 10). Frequency holes show no such latitudinal trend (results 2, 3, 4, and 10).

Discussion

Effects of the CMB

Regarding the effects of the CMB on PKiKP spectra during transmission through the CMB, we address this issue in the context of the results of previous studies. Using amplitude of precursors to PKIKP, Dai et al. (2012) and Yao and Wen (2014) showed that several regions exhibit weak scattering in the lowermost mantle beneath the southwestern Pacific. PKiKP phases from events that occurred in the Banda Sea (events 4 and 9), Sumatra (events 3 and 10), and the Philippines (event 11) enter a "normal" CMB. According to Hedlin and Shearer (2000), there is a relatively weak scattering region in the lowermost mantle beneath the Philippine Sea, which corresponds to the CMB entry points of PKiKP for events 1 and 5 and the CMB exit points for events 1, 3, 4, 5, 9,

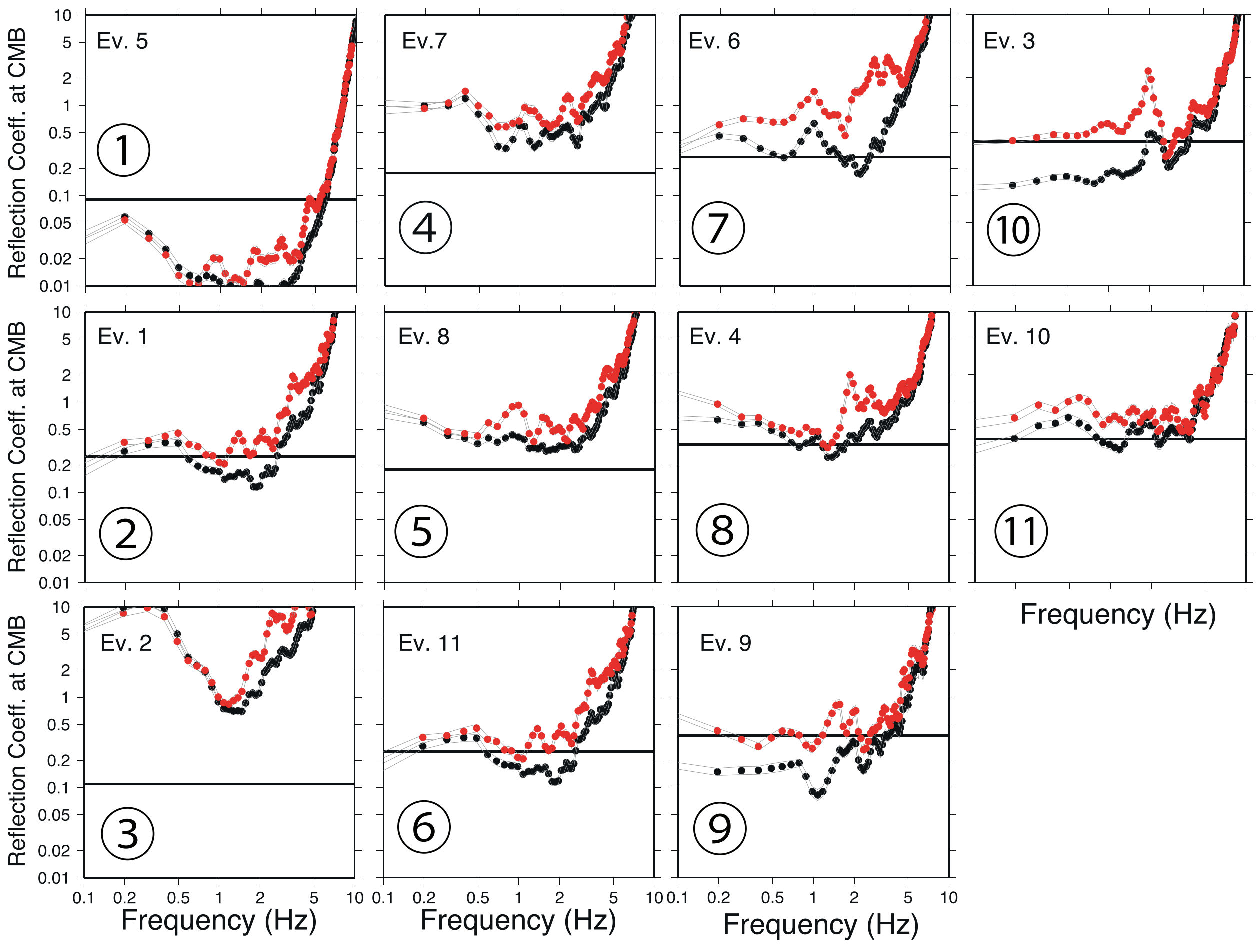

Fig. 7 P wave reflection coefficients at the CMB. P wave reflection coefficients at the CMB as a function of frequency, estimated from PcP/P spectral ratios (*red circles*) and noise/P (*black circles*). *Thin lines* show the upper and lower bounds of standard errors. *Thick lines* are theoretical values of the reflection coefficient calculated using ak135 (Kennett et al., 1995). *Encircled numbers* have the same meaning as in Fig. 6

10, and 11. Thus, we have reason to believe that the CMB effects on the estimated reflection coefficients for results 1, 2, 6, 8, 9, 10, and 11 will be negligible. However, a strong scattering area near the CMB exists beneath north Japan and the northwestern Pacific, which includes the PKiKP CMB entry and exit points for events 2, 6, 7, and 8. Thus, we cannot rule out the possibility that the frequency characteristics of calculated reflection coefficients for results 3, 4, 5, and 7 are CMB effects, e.g., the high-frequency components of PKiKP may be lost by scattering at the CMB.

Numerical simulations

Problem setup

To explain our observations, we use the 2D finite difference program *e3d* (Larsen and Shultz 1995; Rodgers et al. 2006) to simulate wave propagation by solving the full wave equation on a staggered grid. The solutions are fourth order accurate in space and second order accurate in time. Figure 10a shows the configuration of the simulation, for which the grid spacing is 70 m. P- and S-wave velocities and densities above and below the ICB are taken from ak135 (Kennett et al. 1995). We place a sequence of point sources with 1 km spacing on a straight line 100 km long and generate a plane wave. The incidence angle θ is a control parameter. As the input, the representative P wave waveform is taken from the Mariana event (event 1). The calculation is valid for frequencies up to 5 Hz. We examine the observed spectral ratios between incident and reflected waves at three points (triangles in Fig. 10a). To verify the configuration and boundary conditions, and to ensure that there are no unwanted numerical effects from the edges of the box, we conducted a test run of a simple, flat ICB, with elastic parameters on both sides of the ICB taken from the ak135 model (Fig. 10b). The spectral ratios between upgoing and downgoing waves for incidence angles of 10°, 20°, and 30° correspond to epicentral distances of approximately 16°, 32°, and 48°, respectively. Although there are small frequency-dependent fluctuations (within

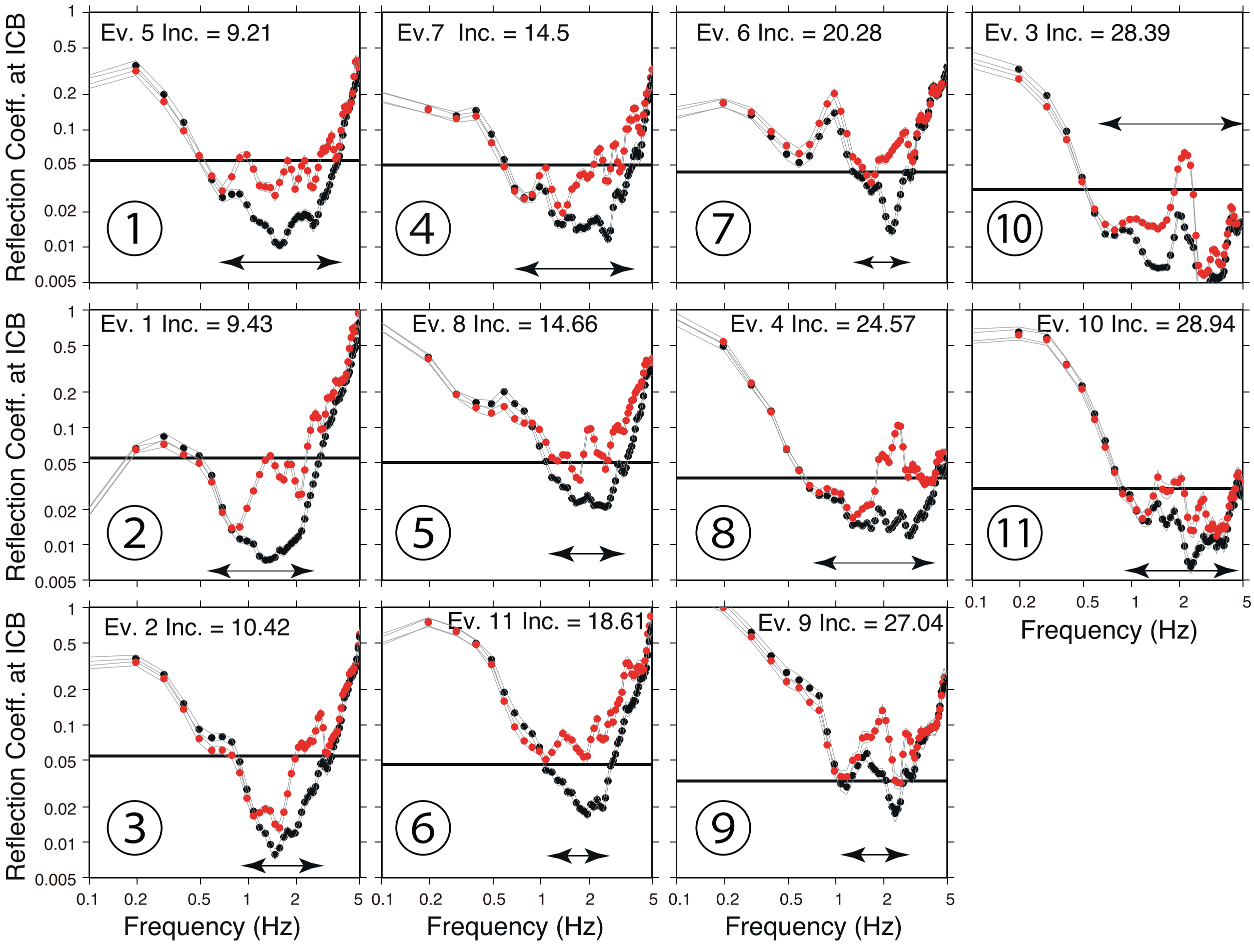

Fig. 8 Corrected P wave reflection coefficients at the ICB. P wave reflection coefficients at the ICB as a function of frequency, estimated from PKiKP/PcP spectral ratios (*red circles*) and noise/PcP (*black circles*). Ratios are corrected for fluctuations estimated from the P wave reflection coefficients at the CMB, obtained from the PcP/P ratios in Fig. 7. *Thin lines* are upper and lower bounds by standard errors. *Thick lines* are theoretical values of the reflection coefficient calculated using ak135 (Kennett et al., 1995). *Horizontal arrows* indicate the effective frequency ranges. *Encircled numbers* are explained in Fig. 6

a factor of 2, at most), their average values coincide well with the theoretical reflection coefficients at the ICB.

Simulations for a thin layer above the ICB

As discussed in the "Background" section, there are multiple conceptual models that can explain freezing and melting of the quasi-eastern hemisphere. To investigate the possibility of a thin layer above the ICB, we run a series of simulations with layer thicknesses of 0.1, 0.25, 0.5, 0.75, 1.0, 3.0, and 5.0 km. For a solid layer above the ICB with finite shear-wave velocity and slight variations in compressional wave velocity and density (Vp = 10.6–10.9 km/s, Vs = 1–3 km/s, ρ = 12.4–12.5 g/cm^3), all the resultant reflected wave amplitudes are small. However, a light or heavy liquid layer (Vp = 9.6–10.3 km/s, ρ = 12.5 g/cm^3 for heavy liquid, ρ = 11.5 g/cm^3 for light liquid) results in large amplitudes. In particular, we find that the amplitudes of seismograms filtered with central frequencies of 1 and 2 Hz become large when we insert a heavy liquid layer above the ICB with Vp = 9.6 km/s, ρ = 12.5 g/cm^3, and a thicknesses of 0.75 or 1 km (Fig. 11a, b). This finding is qualitatively consistent with the results of Krasnoshchekov et al. (2005). However, we also find that spectral ratios continuously increase as a function of frequency for any incidence angle (Fig. 11c), without distinct peaks or holes in the frequency range 0.5 to 3 Hz. Since this does not explain our observations, we reject the model of a thin layer above the ICB as a possible explanation for the observed frequency-domain characteristics of PKiKP.

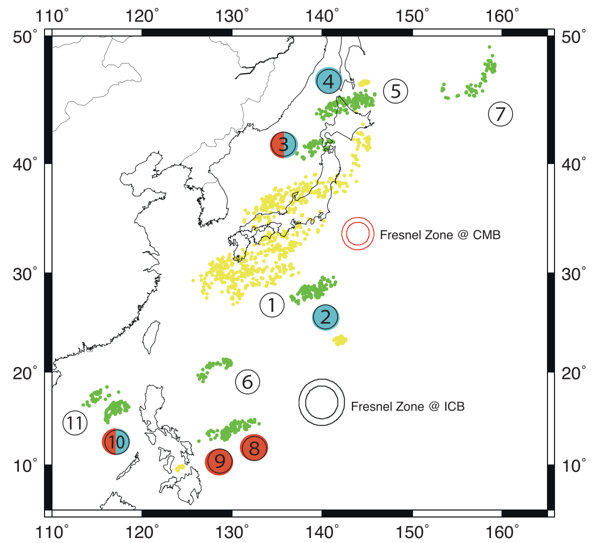

Fig. 9 Summary map of frequency characteristics of P wave reflection coefficients at the ICB. Distribution of the reflection points of PKiKP waves at ICB (*green dots*), and "result numbers" indicating their frequency characteristics by colors. *White*: almost flat spectrum; *blue*: spectrum with a spectral hole; *red*: spectrum with a spectral peak; *half red and blue*: both a hole and a peak. *Yellow dots* indicate the exit and entrance points of PKiKP at the CMB. *Double black and red circles* are Fresnel zones at the ICB and CMB, respectively. *Inner and outer circles* are Fresnel zone estimates for 2 and 1 Hz, respectively

Simulations for topography at the ICB

Earlier PKiKP and PcP amplitude ratio analyses made sporadic seismological observations of a lower density contrast at the ICB than predicted values for spherically symmetric Earth models, as low as 200–300 g/m^3(Koper and Pyle 2004; Tkalčić et al. 2009). In addition, Gubbins et al. (2008) inferred a low density contrast from geodynamical considerations. These results indirectly support the existence of a dense layer at the top of the inner core (F-layer) to explain the smaller density differences between the outer and inner cores. However, there is no proof from seismology that such a layer is a global feature. Masters and Gubbins (2003) noted that even the relatively large density jump inferred from free oscillation analyses is consistent with an F-layer having a strong density gradient: the free oscillation data would average over thick layers below and above the ICB, while the body wave would be sensitive to variations across the ICB. A lower density contrast across the ICB would permit larger topography (Buffett 1997). Of particular interest is the possibility of sharp edges between the solidification and melting areas. Recent waveform modeling suggests significant topography (Dai et al. 2012); however, determination of the amplitude is a more difficult problem than determination of the wavelength.

One possibility of most simplified geometry is that a sinusoidal topographic structure might develop at the largest scales ($\lambda = 10$–100 km) (Buffett 1997). At these length scales, there is an inverse relationship between relaxation time scale and wavelength (Turcotte and Schubert 2002). In addition, the time scale required for topography to relax varies inversely with density contrast and linearly with viscosity. As the viscosity of the outer core is effectively zero (de Wijs et al. 1998), the rate of relaxation is thus entirely controlled by deformation in the inner core.

On the other hand, spike-shaped topographic structures might develop as a result of dendritic growth, likely at smaller scales ($\lambda = 10$–several 100 m) (Bruce Buffett, pers. comm.). Such topography could be relaxed through melting and freezing (thermal relaxation). As the temperature gradients are steeper at short wavelengths, this can drive the heat flow needed to melt or freeze.

Given the above, we test two different classes of topography at the ICB. In the first scenario, we test a regular sinusoidal topography with wavelength λ and height H (Fig. 12a). The values of (λ, H) tested, in kilometers, are (0.1, 0.1), (0.2, 0.2), (0.5, 0.5), (1.0, 1.0), (1.5, 1.5), (2.5, 2.5), (2.5, 2.6), (2.5, 2.7), (5.0, 2.5), and (10.0, 5.0). Figure 13 shows the results of selected combinations of λ and H. The topographies with $\lambda = 0.1$ and 0.2 km and $H = 0.1$ and 0.2 km did not reproduce any spectral peaks and holes and yielded spectra similar to those obtained from a simple discontinuity model (Fig. 10b). However, for a slightly more prominent topography of $\lambda = 0.5$ km and $H = 0.5$ km, we find a clear peak in spectral ratios around 1.2 Hz (Fig. 13a). The ICB topography with $\lambda = 1.0$ and $H = 1.0$ km results in an increased number of spectral peaks (Fig. 13b). The topographic model with $\lambda = 1.5$ and $H = 1.5$ km produces distinct peaks around 2 Hz for incidence angles of 20° and 30° and remarkable holes around 1.2 Hz for incidence angles of 10° and 30° (Fig. 13c). The best results are obtained for the topography characterized by $\lambda = 1.5$ and $H = 1.5$ km. The simulated spectra contain similar characteristics to those observed in the reflection coefficient profiles of results 8, 9, and 10. However, when the longer λ and larger H are used in simulations (e.g., $\lambda =$ 5 and $H = 2.5$ km; $\lambda = 10$ and $H = 5$ km), the reflection coefficients overall become smaller than those for the flat ICB. The spectra are devoid of peaks at higher frequencies (Fig. 13d, e).

Finally, we introduce "spiky" topography to address the possibility of dendritic growth of the inner core (Sumita and Bergman 2009), which is mathematically expressed in our simulations by a reversed cycloid with

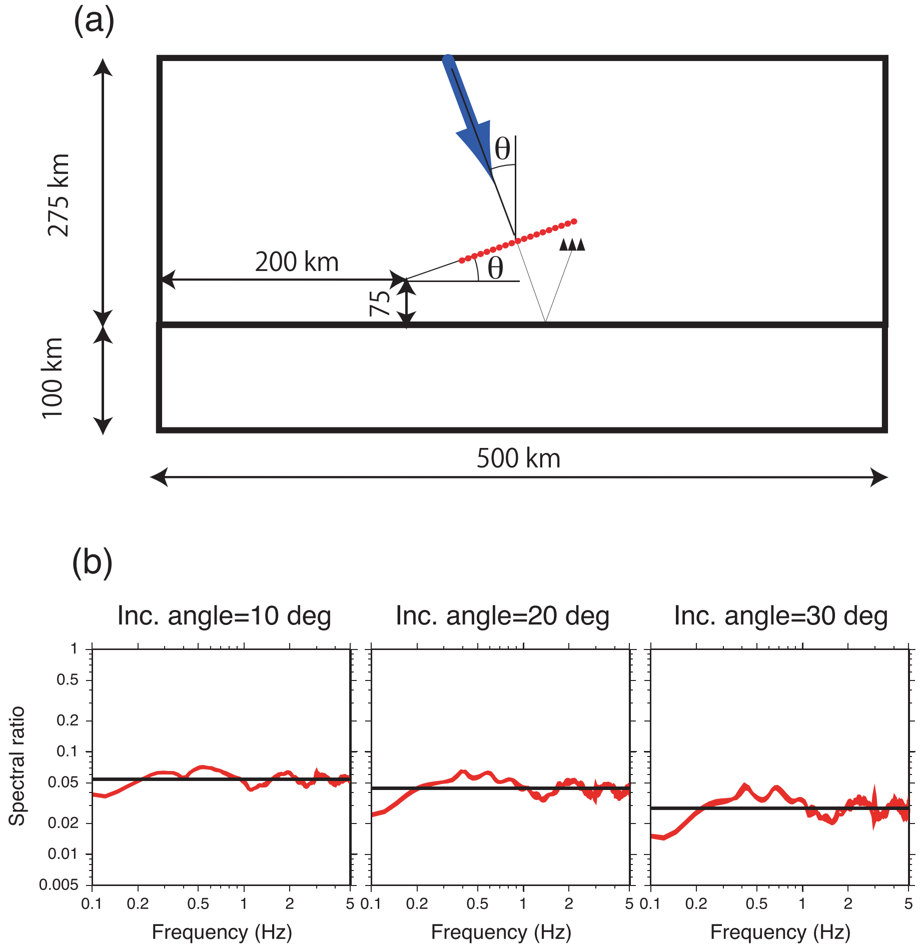

Fig. 10 Configuration of 2D finite difference simulations and a test run. **a** Configuration of 2D finite difference simulations using e3d (Larsen and Shultz 1995). *Small red circles* represent multiple sources used to simulate a plane wave. *Triangles* mark the locations of virtual receivers used to record the reflected waves. Incidence angles θ are a control parameter. **b** Spectral ratios between upward and downward waves using a flat discontinuity in simulations for incidence angles of 10°, 20°, and 30°. *Thick lines* are theoretical values of the reflection coefficient calculated using ak135 (Kennett et al. 1995)

upward sharp tips (Fig. 12b). We tested several (λ, H) combinations for this conceptual model: (0.1, 0.1), (0.2, 0.2), (0.5, 0.2), (0.5, 0.1), (0.5, 0.2), (1.0, 0.2), (1.0, 0.5), (1.0, 1.0), (1.0, 2.0), (1.2, 1.7), (1.5, 1.5), (1.5, 2.0), (2.0, 1.0), (2.0, 1.5), (2.0, 2.0), and (5.0, 2.0). The overall characteristics of the spectral ratios for spiky topography, with $\lambda \leq 2$ km and $H \leq 2$ km (Fig. 14a–d), can be summarized as a gradual decrease in spectral ratio as frequency increases from 0.5 to 5 Hz. This topographic model can explain several peaks or holes for incidence angles of $\theta = 10°$ and 20° and many peaks at frequencies around 2, 3, and 4 Hz for $\theta = 30°$. The topography with $\lambda = 5$ km and $H = 2$ km results in relatively flat and small spectral ratios in the frequency range 0.7–5 Hz. Such a model can explain many holes at frequencies larger than 2.5 Hz for $\theta = 10°$–20° and peaks for $\theta = 30°$. However, these results cannot adequately explain our observations because the overall reflection coefficients are too small.

The resultant characteristics are slightly different from those produced by the sinusoidal topographies, even though their structural dimensions are the same. The frequencies of the distinct spectral peaks decrease with increasing wavelength and height (Fig. 14b–d), whereas no distinct peaks are observed for the topography with $\lambda = H = 0.5$ km. The spiky topography with $\lambda = H = 1.0$ km results in a distinct peak around 1.7 Hz for $\theta = 10°$–20° and a large hole around 1.5 Hz for $\theta = 30°$ (Fig. 14b). The topography with $\lambda = 1.5$ and $H = 1.5$ km yields a distinct single peak at roughly $f = 1.2$ Hz. There are several spectral holes for $\theta = 10°$–20° and peaks for $\theta = 30°$ at $f > 2$ Hz (Fig. 14c). Of all the test cases with spiky topography, the case with $\lambda = H = 1.0$ km most closely matches the observed spectral ratios.

In summary, our observations and numerical simulations suggest that the inner core boundary is a sharp boundary without transitional layers. The hypothesis of

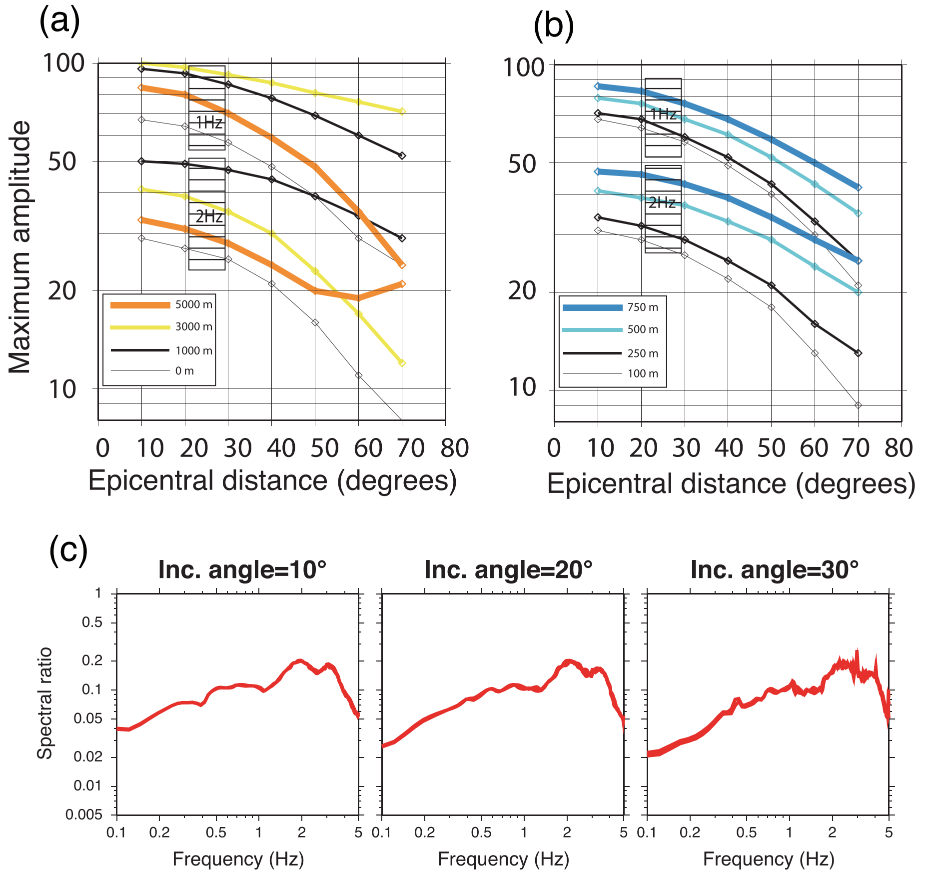

Fig. 11 Results of numerical simulations for a liquid thin layer above the ICB. Maximum amplitudes of the reflected waves measured on seismograms filtered around 1 and 2 Hz as a function of increasing angular distance at the ICB. Synthetic seismograms are calculated by including a heavy liquid layer (Vp = 9.6 km/s, $\rho = 12.5$ g/cm^3) overlying the ICB with varying thicknesses: **a** 0, 1000, 3000, and 5000 m and **b** 100, 250, 500, and 750 m. **c** Spectral ratios for the 1000 m-thick heavy liquid layer for incidence angles of 10°, 20°, and 30°

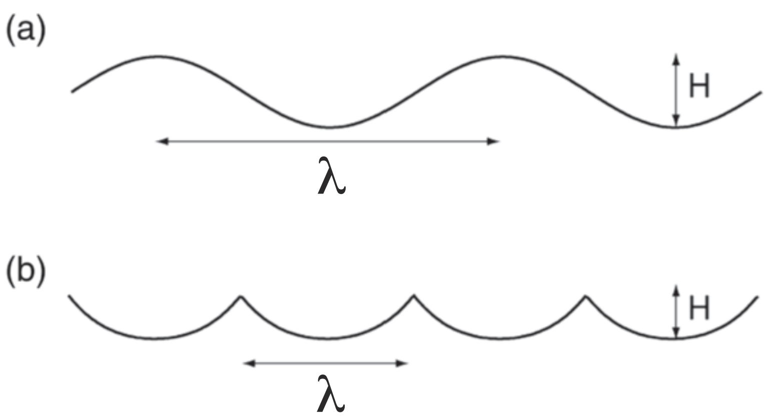

Fig. 12 Diagram of ICB topography. Diagram of ICB topography used in numerical simulations with wavelength and height defined as λ and H, respectively. **a** Sinusoidal topography; **b** "spiky" topography. The meaning of each topographic model is explained in the text

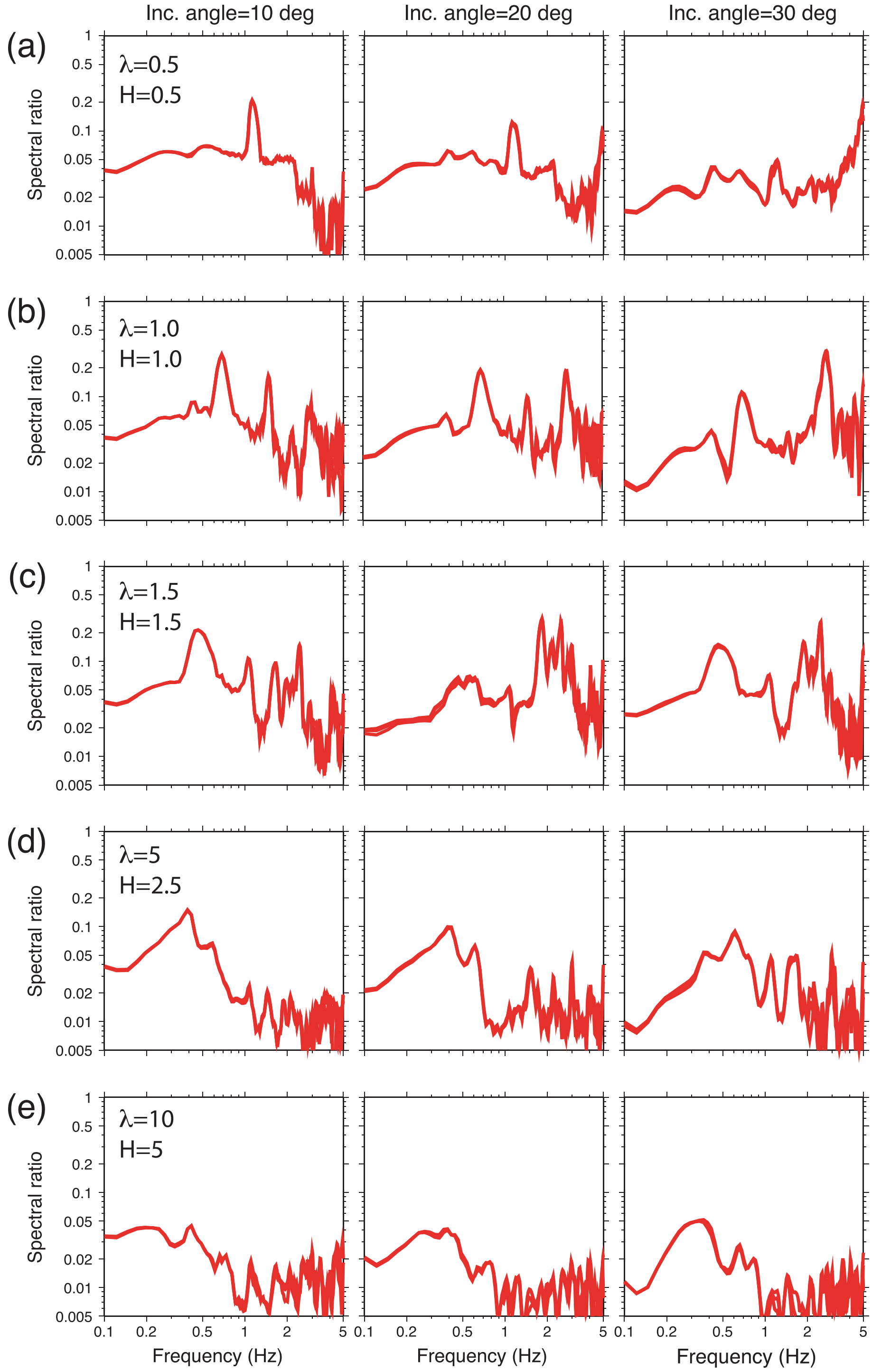

Fig. 13 Results for sinusoidal topographies. Representative results, characterized by height *H* and length *λ*, for incidence angle 10 degrees (*left*), 20 degrees (*middle*) and 30 degrees (*right*). The values of *H* and lambda are as follows: **a**) $\lambda = 0.5$, H = 0.5, **b**) $\lambda = 1.0$, $H = 1.0$, **c**) $\lambda = 1.5$, $H = 1.5$, **d**) $\lambda = 5$, $H = 2.5$, **e**) $\lambda = 10$ $H = 5$

melt at the surface of the inner core in the quasi-eastern hemisphere is not supported by our simulations. The most likely scenario to explain some of the observed spectral characteristics is the existence of topography at the ICB; however, more than one class of topography must be invoked to explain all observations. We therefore conclude that the topography characteristics of the ICB vary laterally. These variations may result from

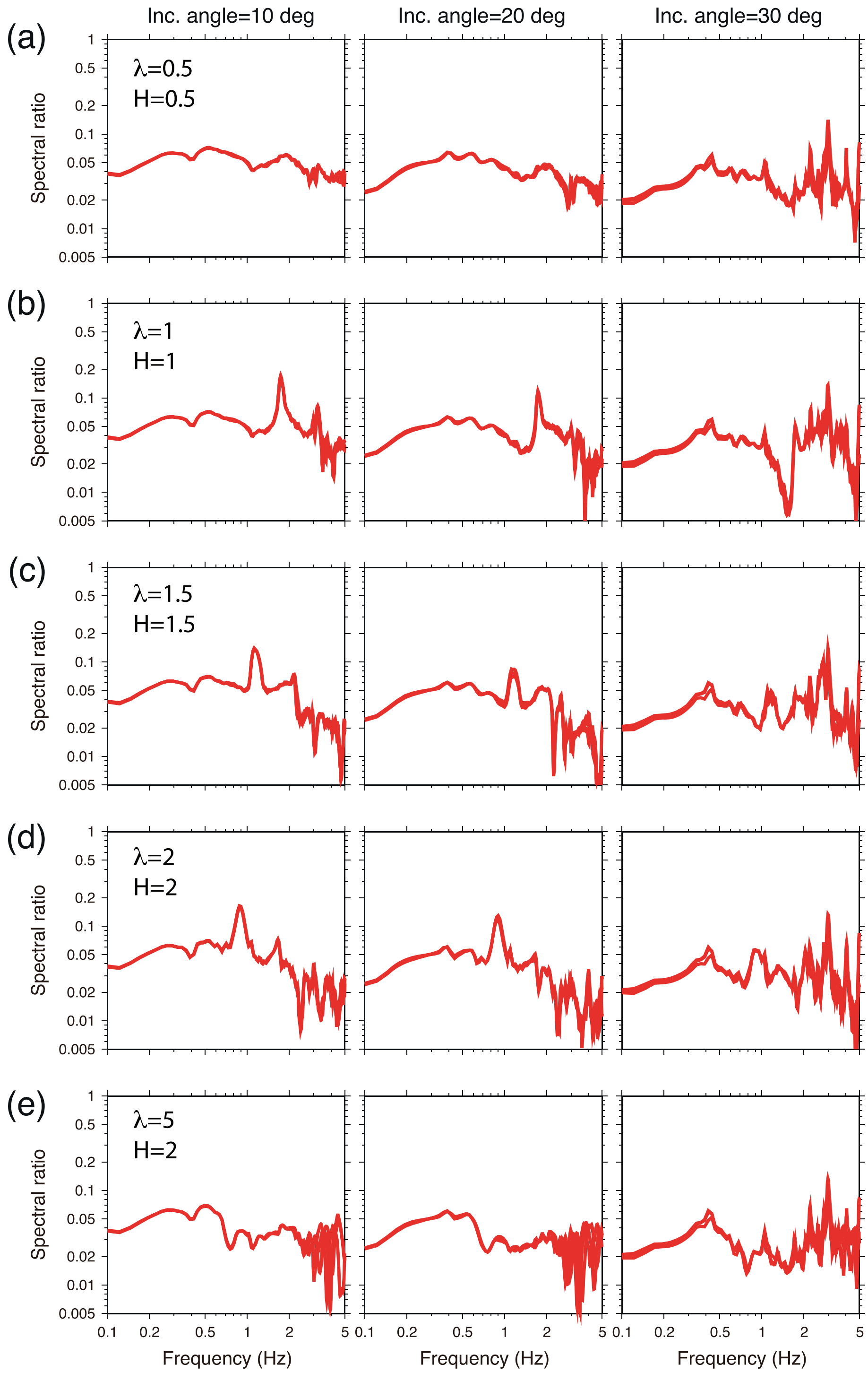

Fig. 14 Results for spiky topographies. Same as Fig. 13, but "spiky" topography was used in simulations. The values of *H* and *λ* are as follows: **a**) $\lambda = 0.5$, $H = 0.5$, **b**) $\lambda = 1$, H=1, **c**) $\lambda = 1.5$, $H = 1.5$, **d**) $\lambda = 2$, $H = 2$, **e**) $\lambda = 5$ $H = 2$

lateral variations of inner core solidification. If solidification is dynamically driven from top to bottom, its geographical pattern will be controlled by the pattern of outer core convection (Bergman et al. 2002; Aubert et al. 2008; Gubbins et al. 2011). If the solidification is instead driven from the bottom up, the pattern will be affected by variations in inner core convection (Deguen and Cardin 2011). Furthermore, small-scale variations in topographic characteristics suggest small-scale convection in a mushy zone at the ICB (Bergman and Fearn

1994; Deguen et al. 2007). While we cannot distinguish between these hypotheses in the present study, largely due to the fact that we sample only sparse and limited areas of the ICB, further observations of PKiKP and PcP will improve our understanding of large-scale ICB structure and dynamics.

Conclusions

Frequency characteristics of ICB reflection coefficients were investigated for the area around Japan using Hi-net vertical component seismograms. We found four patterns in the frequency-dependent behavior of reflection coefficients: (a) a nearly flat spectrum (little variation), (b) a significant hole at a frequency of approximately 1 or 3 Hz, (c) a peak at a frequency of approximately 2 or 3 Hz, and (d) the existence of a hole and a peak. The variety in observed spectra reflects the complex nature of the ICB. To interpret these observations, we conducted 2D finite difference simulations. Since we tested only limited cases with planar geometry, further simulations are required. Our modeling results suggest that holes and peaks in the spectra of reflection coefficients can be qualitatively explained by a sinusoidal or spike-like topography at the ICB, with wavelengths and heights ~1–1.5 km, whereas a liquid or solid layer overlying the ICB does not reproduce any of the observed spectral features.

Abbreviations
CMB: core–mantle boundary; ICB: inner core boundary.

Competing interests
The authors declare that they have no competing interests.

Authors' contributions
ST analyzed waveform data. HT performed finite difference simulations. The manuscript was written by ST and HT. Both authors read and approved the final manuscript.

Authors' information
ST is Deputy Director and Senior Scientist at the Department of Deep Earth Structure and Dynamics Research, Japan Agency for Marine-Earth Science and Technology.
HT is Associate Professor and Senior Fellow at Seismology and Mathematical Geophysics, Research School of Earth Sciences, The Australian National University.

Acknowledgements
The authors are grateful to the National Research Institute for Earth Science and Disaster Prevention (NIED), Japan, for providing high-quality seismograms recorded by the high-sensitivity seismograph network (Hi-net). The authors thank two anonymous reviewers who give valuable comments. S.T. was supported in part by MEXT KAKENHI grant number 15H05832. H.T. was supported by the Japan Society for the Promotion of Science and the Research School of Earth Science, The Australian National University during his stay in Japan. Most of the figures were drawn using GMT (Wessel and Smith 1998).

Author details
[1]Department of Deep Earth Structure and Dynamics Research, Japan Agency for Marine-Earth Science and Technology, Yokosuka 237-0061, Japan.
[2]Research School of Earth Sciences, The Australian National University, Canberra ACT 2601, Australia.

Received: 21 April 2015 Accepted: 8 October 2015
Published online: 04 November 2015

References
Alboussiere T, Deguen R, Melzani M (2010) Melting-induced stratification above the Earth's inner core due to convective translation. Nature 466:744–9
Aubert J, Amit H, Hulot G, Olson P (2008) Thermochemical flows couple the Earth's inner core growth to mantle heterogeneity. Nature 454:758–62
Bergman MI, Fearn DR (1994) Chimneys on the Earth's inner-outer core boundary. Geophys Res Lett 21:477–80
Bergman MI, Cole DM, Jones JR (2002) Preferred crystal orientations due to melt convection during directional solidification. J. Geophys. Res., 107: doi:10.1029/2001JB000601
Buchbinder GGR (1972) Travel times and velocities in the outer core from PmKP. Earth Planet Sci Lett 14:161–8
Buffett BA (1997) Geodynamic estimates of the viscosity of the Earth's inner core. Nature 388:571–3
Cao A, Romanowicz B (2004) Constraints on density and shear velocity contrast at the inner core boundary. Geophys J Int 157:1146–51
Cormier VF (2007) Texture of the uppermost inner core from forward- and back-scattered seismic waves. Earth Planet Sci Lett 258:442–53
Creager KC (1999) Large-scale variations in inner core anisotropy. J Geophys Res 104:23127–39
Cummins P, Johnson L (1988) Synthetic seismograms for an inner core transition of finite thickness. Geophys J 94:21–34
Dai Z, Wang W, Wen L (2012) Irregular topography at the Earth's inner core boundary. Proc Natl Acad Sci 109:7654–8
de Wijs GA, Kresse G, Vocadlo L, Dobson DP, Alfè D, Gillan M, Price GD (1998) The viscosity of liquid iron at the physical conditions of the Earth's core. Nature 392:805–7
Deguen R (2012) Structure and dynamics of Earth's inner core. Earth Planet Sci Lett 333–334:211–25
Deguen R, Cardin P (2011) Thermochemical convection in Earth's inner core. Geophys J Int 187:1101–18
Deguen R, Alboussiere T, Brito D (2007) On the existence and structure of a mush at the inner core boundary of the Earth. Phys Earth Planet Inter 164:36–49
Deuss A (2014) Heterogeneity and anisotropy of Earth's inner core. Ann Rev Earth Planet Sci 42:103–26
Deuss A, Irving JCE, Woodhouse JH (2010) Regional variation of inner core anisotropy from seismic normal mode observations. Science 328:1018–20
Engdahl ER, Flinn EA, Romney CF (1970) Seiemic waves reflected from the Earth's inner core. Nature 228:852–3
Engdahl ER, Flinn EA, Massé RP (1974) Differential PKiKP travel times and the radius of the inner core. Geophys J R Astron Soc 39:457–63
Gubbins D, Masters G, Nimmo F (2008) A thermochemical boundary layer at the base of Earth's outer core and independent estimate of core heat flux. Geophys J Int 174:1007–18
Gubbins D, Sreenivasan B, Mound J, Rost S (2011) Melting of the Earth's inner core. Nature 473:361–3
Hedlin MAH, Shearer PM (2000) An analysis of large-scale variations in small-scale mantle heterogeneity using global seismographic network recordings of precursors to PKP. J Geophys Res 105:13655–73
Jiang G, Zhao D (2012) Observation of high-frequency PKiKP in Japan: insight into fine structure of inner core boundary. J Asian Earth Sci 59:167–84
Kawakatsu H (2006) Sharp and seismically transparent inner core boundary region revealed by an entire network observation of near-vertical PKiKP. Earth Planets Space 58:855–63
Kennett BLN, Engdahl ER, Buland R (1995) Constraints on seismic velocities in the Earth from travel-times. Geophys J Int 122:108–24
Kikuchi M, Kanamori H (2003), Note on teleseismic body-wave inversion program, http://www.eri.u-tokyo.ac.jp/ETAL/KIKUCHI/
Koper KD, Dombrovskaya M (2005) Seismic properties of the inner core boundary from PKiKP/P amplitude ratios. Earth Planet Sci Lett 237:680–94
Koper KD, Pyle ML (2004) Observations of PKiKP/PcP amplitude ratios and implications for Earth structure at the boundaries of the liquid core. J. Geophys. Res., 109: doi:10.1029/2003JB002750
Koper KD, Pyle ML, Franks JM (2003) Constraints on aspherical core structure from PKiKP-PcP differential travel times. J Geophys Res 108:2168, doi:2110.1029/2002JB001995

Koper KD, Franks JM, Dombrovskaya M (2004) Evidence for small-scale heterogeneity in Earth's inner core from a global study of PKiKP coda waves. Earth Planet Sci Lett 228:227–41
Krasnoshchekov DN, Kaazik PB, Ovtchinnikov VM (2005) Seismological evidence for mosaic structure of the surface of the Earth's inner core. Nature 435: 483–7
Larsen SC, Shultz CA (1995), E3D:2D/3D Elastic finite-difference wave propagation code, Lawrence Livermore National Laboratory,Livermore, CA, USA. 1–18.
Lay T, Wallace T (1995) Modern global seismology. Academic, San Diego
Leyton F, Koper KD (2007a) Using PKiKP coda to determine inner core structure: 1. Synthesis of coda envelopes using single-scattering theories. J. Geophys. Res., 112: doi:10.1029/2006JB004369.
Leyton F, Koper KD (2007b) Using PKiKP coda to determine inner core structure: 2. Determination of Q_C. J. Geophys. Res., 112: doi:10.1029/2006JB004370.
Leyton F, Koper KD, Zhu L, Dombrovskaya M (2005) On the lack of seismic discontinuities within the inner core. Geophys J Int 162:779–86
Loper DE (1983) Structure of the inner core boundary. Geophys Astrophys Fluid Dyn 25:139–55
Loper DE, Roberts PH (1981) A study of conditions at the inner core boundary of the Earth. Phys Earth Planet Inter 24:302–7
Lythgoe KH, Deuss A, Rudge JF, Neufeld JA (2014) Earth's inner core: Innermost inner core or hemispherical variations? *Earth Planet*. Sci Lett 385:181–9
Masters G, Gubbins D (2003) On the resolution of density within the Earth. Phys Earth Planet Inter 140:159–67
Monnereau M, Calvet M, Margerin L, Souriau A (2010) Lopsided growth of Earth's inner core. Science 328:1014–7
Niu FL, Wen LX (2001) Hemispherical variations in seismic velocity at the top of the Earth's inner core. Nature 410:1081–4
Okada Y, Kasahara K, Hori S, Obara K, Sekiguchi S, Fujiwara H, Yamamoto A (2004) Recent progress of seismic observation networks in Japan –Hi-net, F-net, K-NET and KiK-net–. Earth Planets Space, 56: xv-xxviii
Peng ZG, Koper KD, Vidale JE, Leyton F, Shearer P (2008) Inner-core fine-scale structure from scattered waves recorded by LASA. J. Geophys. Res., 113: doi:10.1029/2007jb005412
Poupinet G, Kennett BLN (2004) On the observation of high frequency PKiKP and its coda in Australia. Phys Earth Planet Inter 146:497–511
Press WH, Teukolsky SA, Vetterling WT, Flannery BP (1988) Numerical recipes in C: the art of scientific computing. Cambridge University Press, Cambridge
Rodgers A, Tkalčić H, McAllen D (2006) Seismic ground motion and site response in Las Vegas Valley, Nevada from NTS explosions and earthquake data. Pure Appl Geophys 163:55–80
Schweitzer J, Kværna T (1999) Influence of source radiation patterns on globally observed short-period magnitude estimates (m_b). Bull Seism Soc Am 89: 342–7
Shearer P, Masters G (1990) The density and shear velocity contrast at the inner core boundary. Geophys J Int 102:491–8
Shimizu H, Poirier JP, Le Mouël JL (2005) On crystallization at the inner core boundary. Phys Earth Planet Inter 151:37–51
Souriau A (2007) Deep Earth structure—the Earth's cores. In: Romanowicz B, Dziewonski AM (eds) Treatise on geophysics, vol. 1, seismology and structure of the Earth. Elsevier, Amsterdam, pp 655–93
Souriau A, Souriau M (1989) Ellipticity and density at the inner core boundary from subcritical PKiKP and PcP data. Geophys J Int 98:39–54
Sumita I, Bergman M (2009) Inner-core dynamics. In: Olson P (ed) Treatise on geophysics, vol. 8, core dynamics. Elsevier, Amsterdam, pp 299–318
Sumita I, Olson P (1999) A laboratory model for convection in Earth's core driven by a thermally heterogeneous mantle. Science 286:1547–9
Takemura S, Furumura T, Maeda T (2015) Scattering of high-frequency seismic waves caused by irregular surface topography and small-scale velocity inhomogeneity. Geophys J Int 201:459–74
Tanaka S, Hamaguchi H (1997) Degree one heterogeneity and hemispherical variation of anisotropy in the inner core from PKP(BC)-PKP(DF) times. J Geophys Res 102:2925–38
Tkalčić H (2015) Complex inner core of the Earth: the last frontier of global seismology. Rev. Geophys., 53: doi:10.1002/2014RG000469
Tkalčić H, Kennett BLN, Cormier VF (2009) On the inner-outer core density contrast from PKiKP/PcP amplitude ratios and uncertainties caused by seismic noise. Geophys J Int 179:425–43
Tkalčić H, Cormier VF, Kennett BLN, He K (2010) Steep reflections from the earth's core reveal small-scale heterogeneity in the upper mantle. Phys Earth Planet Inter 178:80–91
Tkalčić H, Chen Y, Liu R, Huang Z, Sun L, Chan W (2011) Multistep modelling of teleseismic receiver functions combined with constraints from seismic tomography: crustal structure beneath southeast China. Geophys J Int 187:303–26
Turcotte D, Schubert G (2002) Geodynamics, 2nd edn. Cambridge University Press, Cambridge
Waszek L, Irving J, Deuss A (2011) Reconciling the hemispherical structure of Earth's inner core with its super-rotation. Nat Geosci 4:264–7
Wessel P, Smith WHF (1998) New improved version of generic mapping tools released. EOS Trans Am Geophys Un 79:579
Yao J, Wen L (2014) Seismic structure and ultra-low velocity zones at the base of the Earth's mantle beneath Southeast Asia. Phys Earth Planet Inter 233: 103–11